RESEARCH ARTICLE

ADVANCED ENERGY MATERIALS
www.advenergymat.de

In Situ Dual Crosslinked Composite Quasi-Solid Electrolytes Enable Multiple Continuous Ion Transport Channels for Ultra-Long Cycle and High Load Lithium Metal Batteries

Honghao Liu, Di Li, Yuzi Yang, Yu Lan, Xianming Zhao, Tianyu Zhong, Tao Hu, Songteng Luo, Mengjia Guan, and Yongsheng Li**

Composite quasi-solid electrolytes (CQSEs) have emerged as promising candidates for solid-state lithium metal batteries (SSLMBs) through synergistic integration of inorganic fillers and polymer matrices. However, intrinsic interfacial incompatibility between organic/inorganic phases impedes continuous Li^+ migration pathways, leading to compromised ionic dynamics and cycling stability. In this work, surface-modifiable lithiated zeolite (LiZSM-5) is utilized for functional group grafting and designing a hemiacetal-amine polymer (Trimer) with fast ion conduction. A dual-crosslinked CQSE with multiple continuous Li^+ transport channels through integrated zeolite frameworks and polymeric conduction networks has been obtained by in situ polymerization. Combined experimental and computational analyses reveal that the abundant copolymer chain segments synergistically interact with Lewis acid sites on LiZSM-5, optimizing Li^+ transport pathways to achieve exceptional ionic conductivity (3.7 mS cm^{-1}) and Li^+ transference number (0.89). The optimized CQSE enables ultralong cycling stability exceeding 11 000 h in Li symmetric cells and sustains 800 cycles in $LiNi_{0.8}Co_{0.1}Mn_{0.1}O_2$|CQSE|Li full cells at 0.5 C with high active material loading. Remarkably, 1 Ah soft-pack battery displays excellent cycling stability alongside excellent safety characteristics under mechanical abuse tests. This interfacial engineering strategy provides fundamental insights into constructing continuous ion-transport networks through organic/inorganic phase coordination, suggesting promising avenues for a scalable high-energy-density battery.

1. Introduction

The rapid advancement of global technologies in low-altitude aviation, electric aircraft, intelligent robotics, and space station operations has created unprecedented demands for next-generation energy storage systems with enhanced safety profiles and superior energy density.[1,2] Conventional lithium-ion batteries employing flammable organic liquid electrolytes present critical safety risks, including thermal runaway and combustion hazards,[3,4] driving urgent exploration of safer alternatives. Solid-state lithium metal batteries (SSLMBs) utilizing quasi-solid electrolytes (QSEs) have emerged as a particularly promising solution to address both safety concerns and energy density requirements.[5,6] QSE systems typically combine polymer matrices with liquid electrolyte (LE) components, with poly(ethylene oxide) (PEO),[7,8] poly(vinylidene fluoride) (PVDF),[9] poly(acrylonitrile) (PAN),[10] and poly(methyl methacrylate) (PMMA)[11] being the most extensively investigated polymeric frameworks. Despite their potentials, practical implementation of QSEs faces three primary challenges: 1) limited ionic conductivity at ambient temperatures,[12] 2) elevated interfacial impedance at electrode/electrolyte interfaces,[13] and 3) insufficient ion transport kinetics under low-temperature operation,[14] all of which necessitate fundamental material innovations.

To develop high-performance solid-state electrolytes, the proper incorporation of inorganic fillers into QSEs to address the above challenges is essential. Recent research efforts have focused on developing composite quasi-solid electrolytes (CQSEs) through strategic incorporation of inorganic fillers, combining the advantages of organic flexibility and inorganic stability to achieve enhanced ionic conductivity (>1 mS cm^{-1}), improved electrochemical stability windows (>4.5 V vs Li^+/Li), and excellent electrode compatibility.[15,16] Two predominant filler categories have emerged: electrochemically active materials

H. Liu, Y. Yang, Y. Lan, X. Zhao, T. Zhong, T. Hu, S. Luo, M. Guan, Y. Li
Lab of Low-Dimensional Materials Chemistry
Key Laboratory for Ultrafine Materials of Ministry of Education
Frontier Science Center of the Materials Biology and Dynamic Chemistry
Shanghai Engineering Research Center of Hierarchical Nanomaterials
School of Materials Science and Engineering
East China University of Science and Technology
Shanghai 200237, China
E-mail: guanmj@ecust.edu.cn; ysli@ecust.edu.cn
D. Li
School of Energy and Power Engineering
Nanjing University of Science and Technology
Nanjing 210094, China

The ORCID identification number(s) for the author(s) of this article can be found under https://doi.org/10.1002/aenm.202501350

DOI: 10.1002/aenm.202501350

(e.g., LLZO, NASICON-type ceramics)[17,18] and cost-effective inert fillers (e.g., SiO_2, Al_2O_3 nanoparticles).[19,20] The latter category enhances Li^+ transport through dual mechanisms: disrupting polymer crystallinity to create amorphous domains and facilitating Lewis acid-base interactions with both polymer chains and Li^+.[21,22] In recent years, the incorporation of structurally well-defined porous materials—including metal–organic frameworks (MOFs), zeolitic imidazolate frameworks (ZIFs), covalent organic frameworks (COFs), and aluminosilicate zeolites—into polymer-based matrices has attracted considerable attention.[23,24] These materials possess ordered pore structures, high surface areas, tunable chemical environments, and abundant Lewis acid-base sites, which together contribute to enhanced ion dissociation, directional Li^+ transport, and structural integrity within composite electrolytes.[25] ZIF-8, as a representative MOF, has been incorporated into PEO and poly(vinylidene fluoride-co-hexafluoropropylene) PVDF-HFP matrices, where it effectively suppresses polymer crystallinity, immobilizes anions through Lewis acid-base interactions, and facilitates the formation of interconnected ion-conduction pathways.[26] COF-based fillers, characterized by their thermal stability and structural tunability, have also been employed to construct tailored Li^+ transport networks in CQSEs.[27] Zeolites, which feature rigid microporous frameworks and high ion-exchange capacities, have demonstrated effectiveness in enhancing ionic conductivity and thermal stability in such systems.[28] Despite these advances, the widespread application of porous framework-based CQSEs remains limited by issues such as filler agglomeration, phase incompatibility, and incomplete understanding of polymer-filler interfacial transport behavior.[29] Therefore, the rational design of filler surface properties and the optimization of Li^+ transport pathways at heterogeneous interfaces are crucial for further advancement of this class of materials.

Compared with other porous materials such as MOFs and COFs, aluminosilicate zeolites exhibit superior structural rigidity, thermal and chemical stability, and scalability in synthesis. These frameworks, constructed from oxygen-bridged SiO_4 and -AlO_4 tetrahedra, provide highly ordered microporous channels and strong Lewis acid-base characteristics, making them suitable candidates for promoting ion transport in polymer electrolytes.[30,31] Their capacity to disrupt polymer crystallinity, increase the concentration of dissociated Li^+, and stabilize interfacial architectures has rendered them cost-effective and functionally versatile fillers for QSEs.[32] Wu et al.[33] developed a composite solid electrolyte by integrating lithiated zeolites with PVDF-HFP, where the zeolite component reduced polymer crystallinity and liberated more desolvated Li^+, achieving an enhanced ionic conductivity of 1.98×10^{-4} cm S^{-1}. Nevertheless, the interfacial incompatibility between the inorganic filler and the polymer matrix induces electron localization, Li^+-deficient space charge layers due to high potential difference and strong electron transfer, which slows down the multiphase interfacial dynamics and hinders the Li^+ transport in the CQSEs, limiting the further improvement of the ionic conductivity.[34,35] To address these limitations, Yu's group[36] engineered a PVEC/SiO_2 composite electrolyte with hydrogen-bonding-enhanced electrochemical stability. Similarly, Wang et al.[37] developed Kevlar nanofibers functionalized with negatively charged groups to bridge MOF pores, establishing 3D ion-transport networks for improved interfacial Li^+ migration. However, a prevalent research gap persists where the fundamental mechanisms of Li^+ transport across electrode/electrolyte interfaces remain insufficiently addressed in current methodologies. This critical oversight directly manifests as compromised ionic transport efficiency and exacerbated interfacial resistance, fundamentally constraining the electrochemical performance of SSLMBs.[38–40] Therefore, constructing continuous ion-conduction channels between inorganic fillers and polymer electrolytes while synchronously optimizing Li^+ transport pathways across electrode/electrolyte interfaces remains a formidable challenge.

Conventional CQSE fabrication through ex situ membrane assembly frequently results in poor electrode/electrolyte interfacial compatibility and compromised Li^+ transport kinetics.[41] In situ polymerization strategies have emerged as promising solutions, where liquid-state electrolyte precursors are injected into battery cells and solidified under thermal/photo conditions, transforming traditional two-phase interfaces into integrated contact architectures.[42] However, the prevalent use of linear polymers in current in situ systems leads to thermal/electrochemical instability and exacerbated interfacial side reactions.[43] Crosslinked polymer architectures demonstrate superior potential by reducing crystalline domains, enhancing room-temperature ionic conductivity, and improving oxidative stability and mechanical flexibility.[44] Notably, the synergistic combination of crosslinked polymers with covalently bonded porous inorganic fillers for in situ polymerized CQSEs has not yet been systematically explored.

Herein, we present an original design of in situ polymerized CQSEs (denoted as PTHLZ) featuring dual crosslinked centers: 1) surface-modified lithiated ZSM-5 zeolite (LiZSM-5) with abundant Lewis acid sites serves as an inorganic crosslinked center, effectively anchoring PF_6^- anions while reducing polymer crystallinity and liberating mobile Li^+ through its 3D framework; 2) a kind of polymer (Trimer) with hemiacetal amine groups acts as an organic crosslinked center, providing strong Li^+ dissociation capability and rapid ion-conduction pathways through flexible chain segments. Poly(ethylene glycol) diacrylate (PEGDA) is employed as a chain extender to establish multiple continuous ion-transport channels. This dual crosslinked strategy not only constructs an interconnected 3D ion-conduction network, but also simultaneously addresses phase separation issues and electrode/electrolyte interfacial incompatibility. Molecular dynamics simulations combined with electrochemical characterizations reveal enhanced interfacial Li^+ transport mechanisms through multiple fast-ion channels. The optimized PTHLZ achieves a remarkable Li^+ transference number of 0.89 and ionic conductivity of 3.7 mS cm^{-1} at 25 °C. Corresponding lithium symmetric cells demonstrate ultralong cycling stability over 11 000 h at 5 mA cm^{-2}. Practical applications in high-loading $LiFePO_4$ (10.5 mg cm^{-2}) and $LiNi_{0.8}Co_{0.1}Mn_{0.1}O_2$ (NCM811, 17.5 mg cm^{-2}) full cells exhibit extended cycle lives of 1200 and 800 cycles, respectively. Furthermore, soft-pack batteries incorporating PTHLZ display exceptional safety characteristics and cycling durability. This work establishes new paradigms for designing high-performance CQSEs through rational structural engineering.

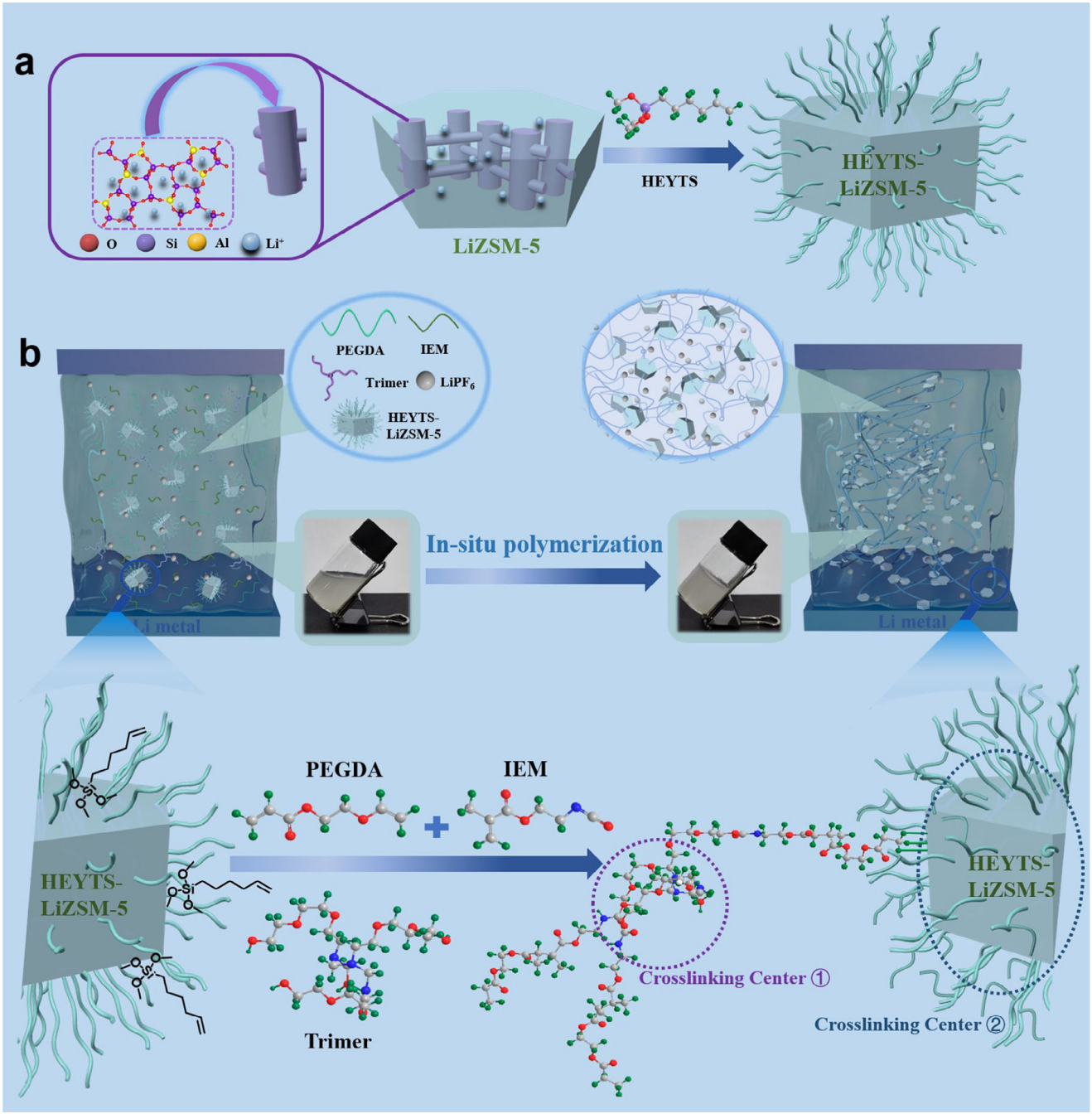

Figure 1. a) Schematic preparation of modified lithiated ZSM-5 (HEYTS-LiZSM-5). b) Design and fabrication of cross-linked composite solid polymer electrolyte PEGDA-Trimer-IEM-HEYTS-LiZSM-5 (named as PTHLZ) by in situ curing.

2. Results and Discussion

Lithiated ZSM-5 zeolites (LiZSM-5) featuring orthorhombic symmetry and a unique 3D pore architecture with mutually perpendicular sinusoidal 10-membered ring channels demonstrate exceptional potential as solid electrolytes, combining molecular sieving capability with an ultra-stable electrochemical window.[45] **Figure** 1a illustrates the stepwise fabrication of HEYTS-LiZSM-5 through three critical stages: i) Li^+ exchange in ZSM-5 via LiCl immersion, ii) surface functionalization using hex-5-en-1-yltrimethoxysilane (HEYTS), and iii) covalent grafting through dehydration between silanol groups and zeolite surface hydroxyls (Figure S1, Supporting Information). This strategic modification preserves the zeolitic framework while introducing reactive vinyl moieties for subsequent polymerization. Then, the soft co-polymer chain with -O-$(CH_2)_2$- chain segments of 2-[2-(2-aminoethoxy)ethoxy]ethanol (NH_2-PEG3-OH) and paraformaldehyde (PFA) as crosslinked agent

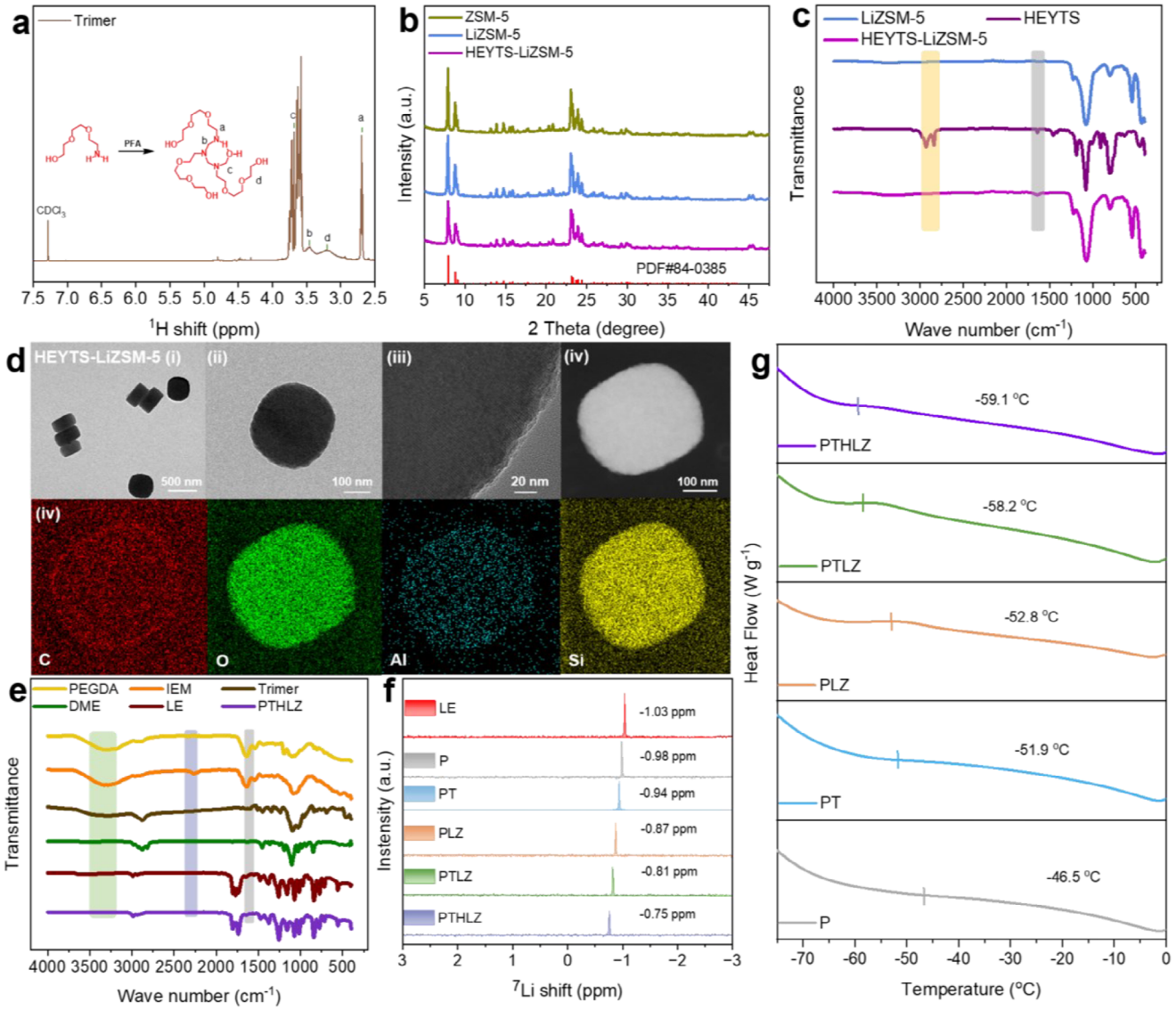

Figure 2. a) ^{1}H NMR spectrum of Trimer. b) XRD patterns of ZSM-5 and HEYTS-LiZSM-5. c) FT-IR spectra of LiZSM-5, HEYTS, and HEYTS-LiZSM-5. d) TEM images of HEYTS-LiZSM-5 at different magnifications (i = 500 nm, ii = 100 nm, and iii = 20 nm) and EDS elemental mapping images iv) of C, O, Si, and Al. e) FT-IR spectra of PTHLZ. f) ^{7}Li NMR spectra of PTHLZ, PTLZ, PLZ, PT, P, and LE. g) DSC curves of PTHLZ, PTLZ, PLZ, PT, and P electrolytes.

was used to form the Trimer with hemiacetal amine crosslinked centers (Figure S2, Supporting Information). 2-Isocyanatoethyl Methacrylate (IEM) was used as a bridging chain to connect the Trimer and enhance the peristaltic properties of the chain segments (Figure S3, Supporting Information). The hemiacetal amine crosslinked center features a weak intramolecular hydrogen bond and relatively strong C—N bond, while the soft phase of the co-polymer chain enables Li^{+} dissociation and rapid transport. As a result, the vinyl groups on the surfaces of Trimer-IEM, poly(ethylene glycol) diacrylate (PEGDA), and LiZSM-5 will undergo in situ polymerization to form a long polymer chain and construct a 3D continuous network structure with LiZSM-5 and Trimer as the dual centers, and the effect is schematically shown in Figure 1b.

First, nuclear magnetic resonance (NMR) analysis confirms the successful synthesis of Trimer. The ^{1}H NMR spectrum (**Figure 2a**) indicates characteristic peaks at 3.69 ppm (-$CH_2NHCH_2N(CH_2)_2$-), 3.47 ppm (-$(CH_2)_2NCH_2N(CH_2)_2$-), and 2.69 ppm (-$OCH_2CH_2NHCH_2$-), supported by mass spectrometry (m/z = 502.3 Da, Figure S4, Supporting Information). X-ray diffraction (XRD) patterns of ZSM-5, LiZSM-5, and HEYTS-LiZSM-5 are presented in Figure 2b. Pristine ZSM-5 displays a pure crystalline phase, while lithium doping (LiZSM-5) preserves the crystallinity, aligning with prior reports.[46] The inductively coupled plasma (ICP) analysis verifies that Li^{+} was successfully loaded into the ZSM-5 framework (Table S1, Supporting Information). The successful grafting of HEYTS onto LiZSM-5 and the preservation of the zeolite framework were

further confirmed by ^{27}Al and ^{29}Si NMR spectroscopy (Figure S5, Supporting Information). The observed decrease in crystallinity likely results from HEYTS hydrolysis, during which HEYTS reacted with surface hydroxyl groups on ZSM-5, self-polymerized, and adhered to the ZSM-5 surface. Fourier transform infrared (FT-IR) spectra (Figure 2c) provided further structural evidence. The HEYTS-LiZSM-5 spectrum features a distinct —CH═CH— vibration at 1641 cm^{-1}, while the disappearance of the —OCH_3 stretching mode at 2937 cm^{-1} confirmed the successful grafting of HEYTS. Meanwhile, scanning electron microscopy (SEM) reveals no significant morphological or size changes in ZSM-5 after proton exchange and functionalization (Figure S6, Supporting Information), indicating structural integrity preservation. Thermogravimetric analysis (TGA) of HEYTS-LiZSM-5 (Figure S7, Supporting Information) shows a 5.3 wt.% mass loss between 258 and 500 °C, attributed to organic group combustion, quantitatively verifying HEYTS grafting. This conclusion was further supported by transmission electron microscopy (TEM) and energy-dispersive spectroscopy (EDS) mapping (Figure S8, Supporting Information). TEM images of HEYTS-LiZSM-5 reveal uniform particles (≈300 nm) with lattice spacings of 1.04 and 1.13 nm (Figure S9, Supporting Information), corresponding to the (101) and (200) planes of ZSM-5, respectively. While EDS confirms the presence of C, O, Si, and Al (Figure 2d), spatial resolution limitations precluded precise organic group localization. To address this, fluorinated F-LiZSM-5 analogs were synthesized using trimethoxy(3,3,3-trifluoropropyl)silane.[46] TEM-EDS mapping (Figure S10, Supporting Information) demonstrates homogeneous F distribution overlapping with Si signals, confirming uniform organic moiety integration within the LiZSM-5 matrix. Brunauer-Emmett-Teller (BET) analysis (Figure S11, Supporting Information) reveals a specific surface area of 499.2 m^2 g^{-1} for HEYTS-LiZSM-5, slightly reduced from pristine ZSM-5 (591.1 m^2 g^{-1}) due to pore occupation by the grafted organic chains.

The FT-IR spectra provided critical insights into the structural evolution of PEGDA-Trimer-HEYTS-LiZSM-5 (named as PTHLZ) during crosslinking. Notably, the weakening of the characteristic —CH═CH— stretching vibration at 1645 cm^{-1} following crosslinking (Figure 2e; Figure S12, Supporting Information), coupled with emerging broad peaks at 3290 cm^{-1} (—OH stretching) and 2267 cm^{-1} (—NCO stretching), confirms that most of the monomers have been successfully converted into long-chain polymers and polymerized with a yield of 83.6%. This interpretation aligns with macroscopic observations (Figures S13 and S14, Supporting Information) showing complete phase transition from liquid precursor to non fluid solid electrolyte, demonstrating the uniformity of HEYTS-LiZSM-5 dispersion in the system. To investigate the effect of each component on the electrochemical properties, a series of cross-experiments were carried out for comparison, and the optimal electrochemical performance mass ratio was 3:1:1 (detailed experiments can be seen in Figures S15 and S16, Supporting Information). The XRD patterns of the PTHLZ and control samples show typical crystal diffraction peaks, confirming the amorphous structure of LiZSM-5 grafted with crosslinked PEGDA and Trimer-IEM (Figure S17, Supporting Information). TGA analysis demonstrated enhanced thermal stability in crosslinked systems, with PTHLZ exhibiting 146.8 °C decomposition temperature (Figure S18, Supporting Information), which is significantly higher than that of the linear PEGDA electrolyte. The amorphous structure promotes segmental vibration and partial relaxation of the polymer chains, thereby facilitating Li^+ transport. Raman analysis (Figure S19, Supporting Information) was performed to investigate the interaction between PTHLZ and $LiPF_6$. The characteristic peaks at 744 and 766 cm^{-1} correspond to free PF_6^- and free EC solvent molecules, respectively.[47] PTHLZ exhibits a significantly higher content of free PF_6^- compared to the other four electrolytes. This observation suggests that both HEYTS-LiZSM-5 and Trimer effectively anchor PF_6^-. This anchoring effect promotes $LiPF_6$ dissociation, thereby increasing the concentration of free Li^+. To gain deeper insight into the Li^+ transport mechanism within PTHLZ, ^{7}Li NMR spectroscopy was employed (Figure 2f; Figure S20, Supporting Information). For the PT electrolyte, two distinct peaks are observed, corresponding to Li^+ coordinated with poly (Trimer-IEM-PEGDA) and Li^+ residing in liquid-electrolyte (LE) rich domains.[48] Upon incorporation of HEYTS-LiZSM-5, additional peaks appear at −0.746 and −0.777 ppm in the PTHLZ electrolyte. These are attributed to Li^+ environments within the HEYTS-LiZSM-5–poly (Trimer-IEM-PEGDA) matrix and the zeolitic framework of HEYTS-LiZSM-5. Concurrently, the intensities of signals associated with poly (Trimer-IEM-PEGDA) and LE-rich pores decrease, supporting the redistribution of Li^+ into more coordinated environments. Moreover, the ^{7}Li NMR signal for PTHLZ exhibits the largest downfield shift (up to 0.28 ppm) among all samples, indicating a decrease in electron density around Li^+. This shift is attributed to the strong anchoring interactions within PTHLZ, which facilitate continuous Li^+ transport through interconnected polymer–zeolite networks, significantly enhancing overall ionic conductivity.[49,50] Differences in the thermal transition behavior of PTHLZ, PTLZ, PLZ, PT and P were analyzed using differential scanning calorimetry (DSC). High-performance solid polymer electrolytes utilized in batteries typically have low glass transition temperatures.[51] Figure 2g presents the glass transition temperature (Tg) of PTHLZ at −59.1 °C. This pronounced Tg depression, induced by LiZSM-5 grafting and Trimer-mediated chain crosslinking, effectively suppresses the crystallinity of the polyether phase. The trend of Tg values for different electrolytes obtained from dynamic thermo-mechanical (DMA) analysis is the same as that from DSC (Figure S21, Supporting Information). The introduction of Trimer and HEYTS-LiZSM-5 facilitates enhanced relaxation dynamics in the polymer phase. Notably, the relatively short Trimer side chains contribute to the formation of an extended amorphous percolating microphase, suggesting weakened inter-chain interactions and a significant increase in the amorphous fraction. This microstructural evolution enables more rapid Li^+ transport within the PTHLZ matrix.[52,53]

To evaluate the ionic conductivity of the prepared PTHLZ, electrochemical impedance spectroscopy (EIS) plots of the assembled cells were performed at varying temperatures (**Figure 3**a). The Nyquist plots (Figure S22, Supporting Information) reveal a pronounced decrease in impedance for PTHLZ, PTLZ, PLZ, and P with rising temperature. The ionic conductivity-temperature relationship (Figure 3b) follows Arrhenius behavior, with PTHLZ exhibiting the lowest activation energy (0.45 eV) compared to PEGDA-Trimer-LiZSM-5 (named as PTLZ) (0.49 eV), PEGDA-LiZSM-5 (named as PLZ) (0.53 eV), PEGDA-Trimer (named as

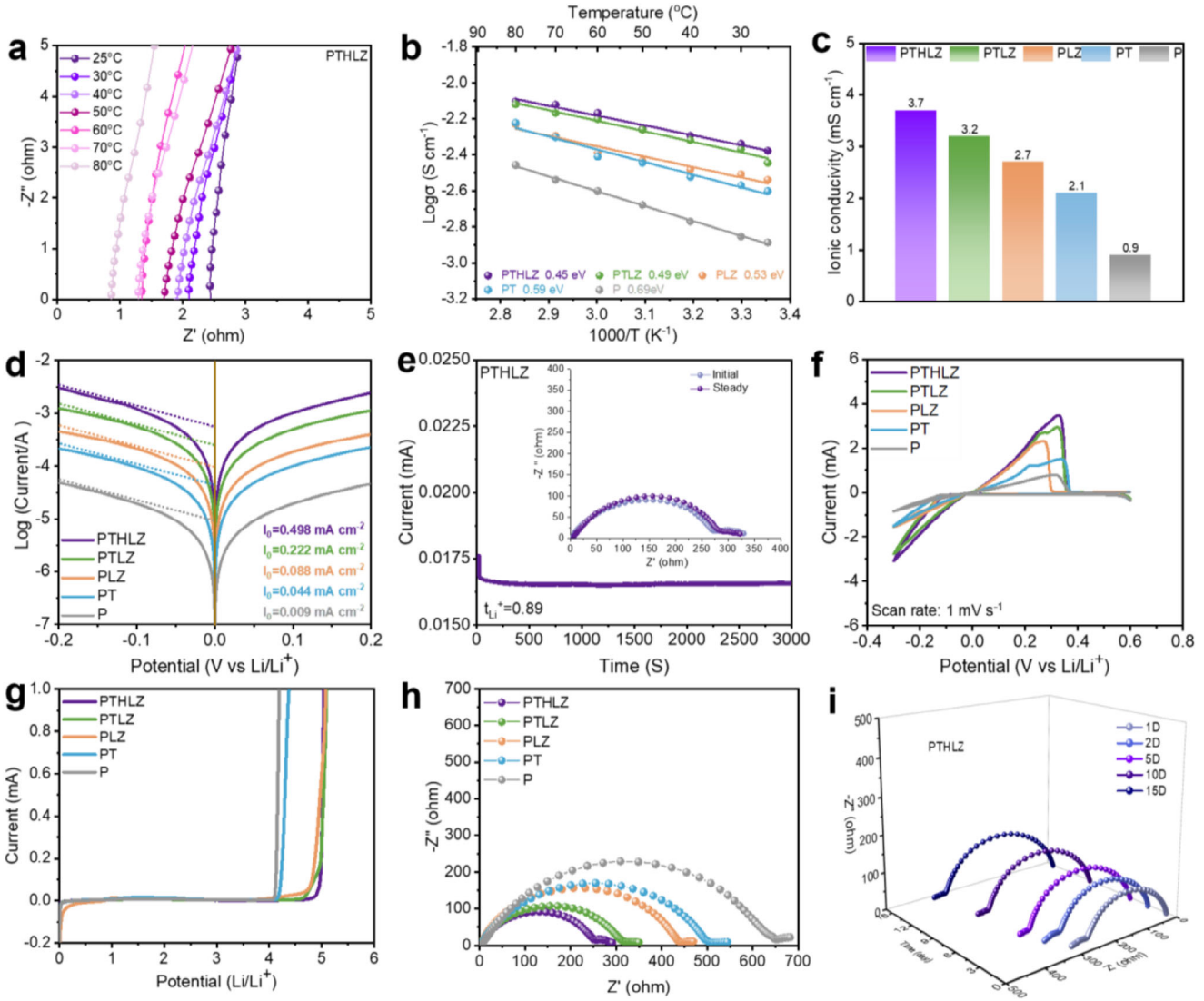

Figure 3. Potential of PTHLZ as a composite solid polymer electrolyte with fast ionic conduction. a) EIS curves of PTHLZ at different temperatures. b) Arrhenius plots of the ionic conductivities of PTHLZ, PTLZ, PLZ, PT, and P. c) Ionic conductivity of PTHLZ, PTLZ, PLZ, PT, and P at room temperature. d) Tafel curves of Li|Li symmetric cells with PTHLZ, PTLZ, PLZ, PT, and P. e) Polarization curves as well as the initial and steady-state impedance diagram of PTHLZ at room temperature (Inset). f) CV curves for PTHLZ, PTLZ, PLZ, PT, and P cells at a scanning rate of 1 mV s^{-1}. g) Linear sweep voltammetry (LSV) curves of PTHLZ, PTLZ, PLZ, PT, and P at room temperature. h) Set of EIS data with PTHLZ, PTLZ, PLZ, PT, and P symmetric cells. i) EIS plot of Li|Li symmetric cells impedance with the variation of time (1–15 days) for PTHLZ.

PT) (0.59 eV), and PEGDA (named as P) (0.69 eV). This reduction in energy barrier for Li^+ migration is attributed to the dual-crosslinked architecture formed by Trimer and HEYTS-LiZSM-5, which establishes multiple ion transport pathways. At room temperature, PTHLZ achieves a superior ionic conductivity of 3.7 mS cm^{-1} (Figure 3c), outperforming all counterparts and underscoring its potential for ambient-condition battery operation. Further, the exchange current density (I_0) of PTHLZ reaches 0.498 mA cm^{-2} (Figure 3d), ≈55-fold higher than that of P (0.009 mA cm^{-2}). This enhancement arises from the 3D continuous Li^+ channels formed by HEYTS-LiZSM-5 and Trimer, which improve the interfacial compatibility via in situ polymerization and stabilize the solid-electrolyte interphase (SEI) on the Li metal anode. The Li^+ transfer number ($t_{Li}{}^+$) of PTHLZ is 0.89 (Figure 3e; Figure S23, Supporting Information), significantly exceeding PTLZ (0.77), PLZ (0.68), PT (0.42), and P (0.24). This improvement stems from 1) anionic interactions between LiZSM-5 and free Li^+, 2) Lewis acid site coordination with Li salts, and 3) anionic hindrance suppression by the dual-crosslinked network.[54] Cyclic voltammetry (CV) of Li|SS cells (Figure 3f) confirms faster charge transfer kinetics in PTHLZ, evidenced by its larger peak area, consistent with its high $t_{Li}{}^+$ and ionic conductivity. Linear scanning voltammetry (LSV) demonstrates an extended electrochemical stability window of 4.8 V for PTHLZ (Figure 3g), surpassing PTLZ and PLZ, which highlights the role of LiZSM-5 structural integrity in enhancing oxidative stability. Excellent interfacial contact between electrodes and electrolyte is crucial for achieving safe and reliable Li metal batteries.[55,56] To

evaluate and compare the EIS between PTHLZ, PTLZ, PLZ, PT, and P QSEs with Li metal anode. As can be seen in Figure 3h, the PTHLZ electrolyte impedance is the smallest (the difference with the P electrolyte is ≈390 Ω). The interfacial impedance of PTHLZ increases from 260 Ω on the first day to 353 Ω on the 15th day, whereas the interfacial impedance of PTLZ, PLZ, PT, and P all increase by more than 250 Ω, with the maximum increment of 1124 Ω (Figure 3i; Figure S24, Supporting Information). The results show that PTHLZ has better contact with the Li metal anode while linear polymers have poor stability to Li metal. In addition, the in situ polymerization strategy improves the compatibility at the electrolyte/electrode interface and among components, which is the prerequisite for stable cycling of the Li metal anode.

To gain more insight into the interactions of Trimer, HEYTS-LiZSM-5, PTHLZ and $LiPF_6$ in the electrolyte and the Li^+ transport paths in the electrolyte, the molecular dynamics and electrolyte/electrode stability mechanisms of Li^+ in PTHLZ and the component systems were investigated by density functional theory (DFT) and molecular dynamics (MD) simulations. **Figures** 4a and S25 (Supporting Information) show the highest occupied molecular orbital (HOMO) and lowest unoccupied molecular orbital (LUMO) energies to evaluate the electrochemical reactivity of each component of the electrolyte and its precursor. PTHLZ, possessing the highest LUMO energy (0.214 eV), is therefore inert in SEI film formation during charging (in agreement with XPS findings). Notably, the depressed HOMO level (−6.873 eV) signifies enhanced oxidative stability at high potentials, arising from structural stabilization through LiZSM-5 framework integration and dual-crosslinking architecture. The snapshots of the PT, P, PTHLZ, and PTLZ are shown in Figure 4b–d and Figure S26 (Supporting Information), and the corresponding radial distribution function shows that the Li-O coordination number within the PTHLZ system reaches 3.55, which is higher than that of PTLZ (3.09), PT (2.86), and P (2.63). The increased number reflects a higher concentration of oxygen-containing molecules in the primary solvation shell of Li^+, suggesting that PTHLZ actively facilitates Li^+ transport. This implies that PTHLZ can establish additional Li^+ transport pathways, thereby enhancing the ionic conductivity of the PTHLZ electrolyte system. Subsequently, the electrostatic potential (ESP) values of Trimer, HEYTS-LiZSM-5, PEGDA, PT, PTHLZ, and a representative polymer segment of PTHLZ were calculated to elucidate the charge distribution (Figure 4e). In Trimer and PT, the negative charge is concentrated on the ether oxygen chain segments (blue color near the O atom). Meanwhile, HEYTS-LiZSM-5 has an overall high positive charge, which is more favorable for the adsorption of anions. The ESP analysis of solvent molecules reveals that only ethylene carbonate (EC) displays strong negative electronegativity (Figure S27, Supporting Information), indicating its high affinity for Li^+. In the polymer chain segments of PTHLZ, the negative charge is primarily concentrated on ether-oxygen segments and polyurethane groups. This suggests that Li^+ coordinates with these oxygen-rich functional groups to facilitate Li^+ transport along the polymer chain, which partly explains the high conductivity of PTHLZ at room temperature.

Furthermore, the electron cloud density distributions of PTHLZ and each constituent repeating unit were calculated to further investigate the interaction of Li^+ with PTHLZ, as shown in Figure 4f and Figure S28 (Supporting Information). The binding sites of Trimer, HEYTS-LiZSM-5, PEGDA, and PT with Li^+ were determined based on the electronegativity of the electrostatic potential and the binding energies, all of which are lower than that of PTHLZ (−4.17694 eV). In contrast, the negative charge of PTHLZ was also detected at the O-atoms of the SiO_4 tetrahedron of LiZSM-5, which suggests that PTHLZ interacts with Li^+ through multiple pathways corresponding to diverse Li^+ transport routes. The binding energies of EC, DEC, and DME with Li^+ (−1.98175, −1.86185, and −1.70174 eV) are lower than that of PTHLZ (Figure S29, Supporting Information), indicating that PTHLZ has a stronger interaction with Li^+ and can more effectively penetrate the solvation shell layer of Li^+. Meanwhile, binding energy calculations for PTHLZ and individual components and individual components with PF_6^- (Figure S30, Supporting Information) show that both HEYTS-LiZSM-5 and PT exhibit strong binding energies (−4.5124 and −4.2102 eV). The PTHLZ formed after the combination shows the maximum binding energy of −8.4537 eV, confirming that the affinity of the Lewis acid sites for PF_6^- promotes the dissociation of Li salt and releases more free Li^+. To better visualize Li^+ transport pathways, we conduct density field simulations. The results reveal that Al atoms within the ZSM-5 framework serve as Lewis acid sites that effectively bind PF_6^-. At the polymer-zeolite interface, the Si—O—Si linkages in ZSM-5 promote rapid Li^+ migration. This behavior is driven by a continuous electronegativity gradient formed by oxygen atoms in the poly (Trimer-IEM) chains (—C═O and —C—O—C—), PEGDA segments (—C—O—C—), and HEYTS-LiZSM-5. These electronegative sites create interconnected conduction pathways, facilitating efficient ion transport. Notably, Li^+ density is significantly enriched in HEYTS-LiZSM-5 regions (Figure S32, Supporting Information), confirming the key role of zeolitic oxygen atoms in enhancing Li^+ mobility through coordinated interactions. Overall, the functional groups in both HEYTS-LiZSM-5 and poly (Trimer-IEM-PEGDA) synergistically construct multiple, interconnected ion-conducting channels.[57]

To give clearer indication of Li^+ diffusion at the interface, the interfacial diffusion kinetics analyzed using the simulated cell were assessed by evaluating the mean-square displacements (MSD). The data indicate that Li^+ diffusivity decreases within the internal channels of LiZSM-5 (5.13×10^{-5} and 9.22×10^{-6} cm^2 s^{-1}), whereas Li^+ tends to accumulate and diffuse more readily outside the framework (1.76×10^{-2} cm^2 s^{-1}) (Figure S32, Supporting Information). Furthermore, the slip-assisted diffusion of Li^+ along the PTHLZ polymer chains in isotropic regions demonstrates significantly enhanced diffusivity (2.21×10^{-1} cm^2 s^{-1}) and promotes ion transport within LiZSM-5 (9.93×10^{-5} and 2.09×10^{-6} cm^2 s^{-1}) (Figure 4h,i). The formation of electron localization at the LiZSM-5 interface greatly reduces the Li^+ migration kinetics. The PTHLZ coherent zone formed by in situ polymerization can effectively inhibit electron localization at the interface, enabling a continuous and fast ion channel. The Li^+ transport channel in the PTHLZ is shown in Figure 4j. The schematic illustrates the structure of the PTHLZ network with Trimer-IEM-PEGDA acting as the soft 3D framework and HEYTS-LiZSM-5 acting as the hard 3D framework, which are crosslinked to form the spatial network of double crosslinked sites. LiZSM-5 facilitates Li salt decomposition and ion transport by generating the free space accommodating Li salt or other poly-

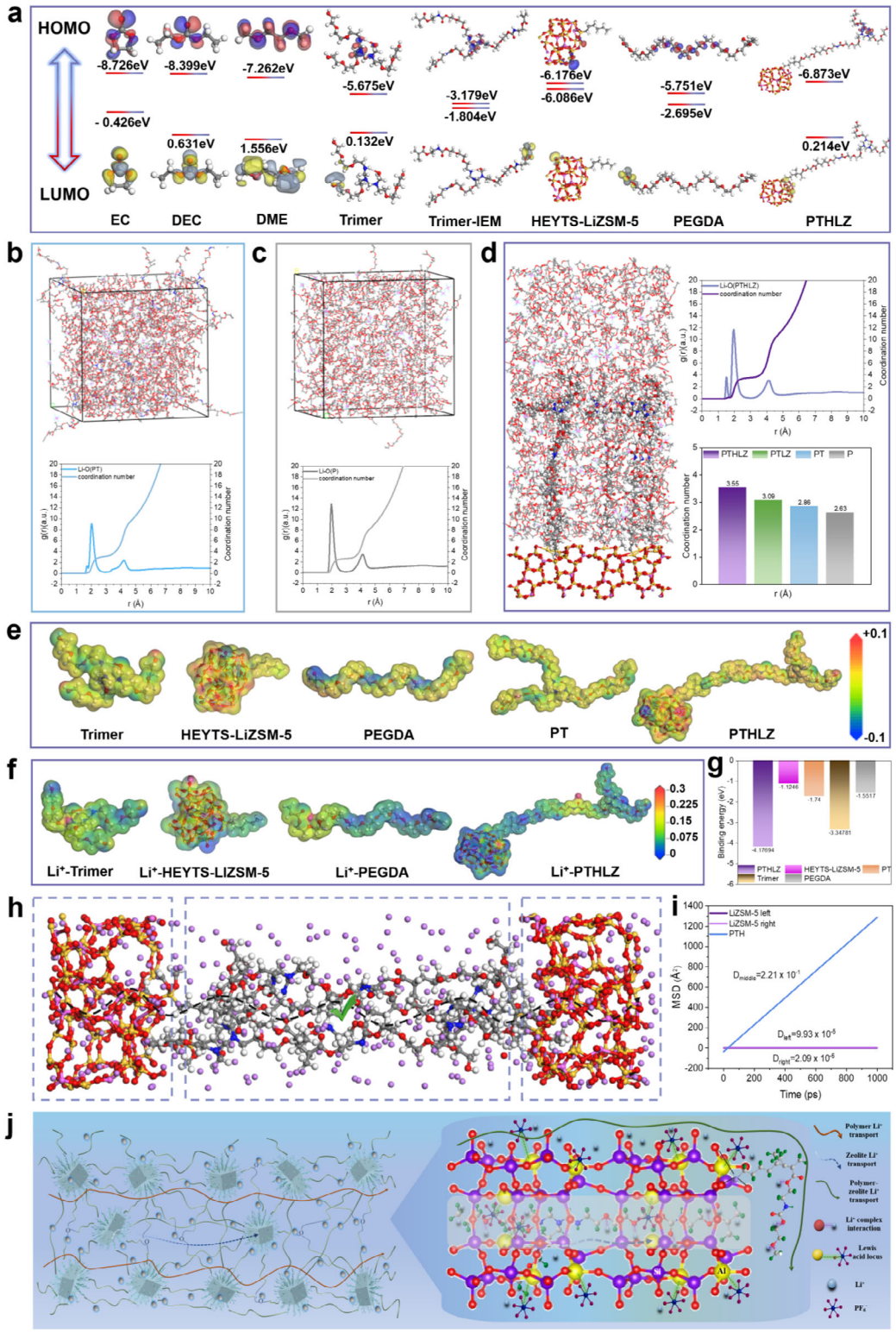

Figure 4. a) Diagram of the LUMO and HOMO energy levels and the corresponding optimized geometrical structures of EC, DEC, DME, Trimer, Trimer-IEM, HEYTS-LiZSM-5, PEGDA and PTHLZ. Snapshots obtained from MD simulations of the PT electrolyte b), P electrolyte c), and PTHLZ electrolyte d) with the corresponding radial distribution functions and statistical diagram of the coordination number of PTHLZ, PT, PTLZ, and P (insert). e) ESP maps of Trimer, HEYTS-LiZSM-5, PEGDA, PT, and PTHLZ. f) Simulations on electron cloud density distributions and g) corresponding binding energies of HEYTS-LiZSM-5, Trimer, PEGDA, and PTHLZ with Li^+. h) Li^+ trajectories for LiZSM-5 with the modification of HEYTS interfacial simulation cells plotted over a 100 ps MSD window. i) The calculated Li^+ diffusivity for LiZSM-5 with the modification of PTHLZ. j) Schematic diagram of ion transport in PTHLZ electrolyte.

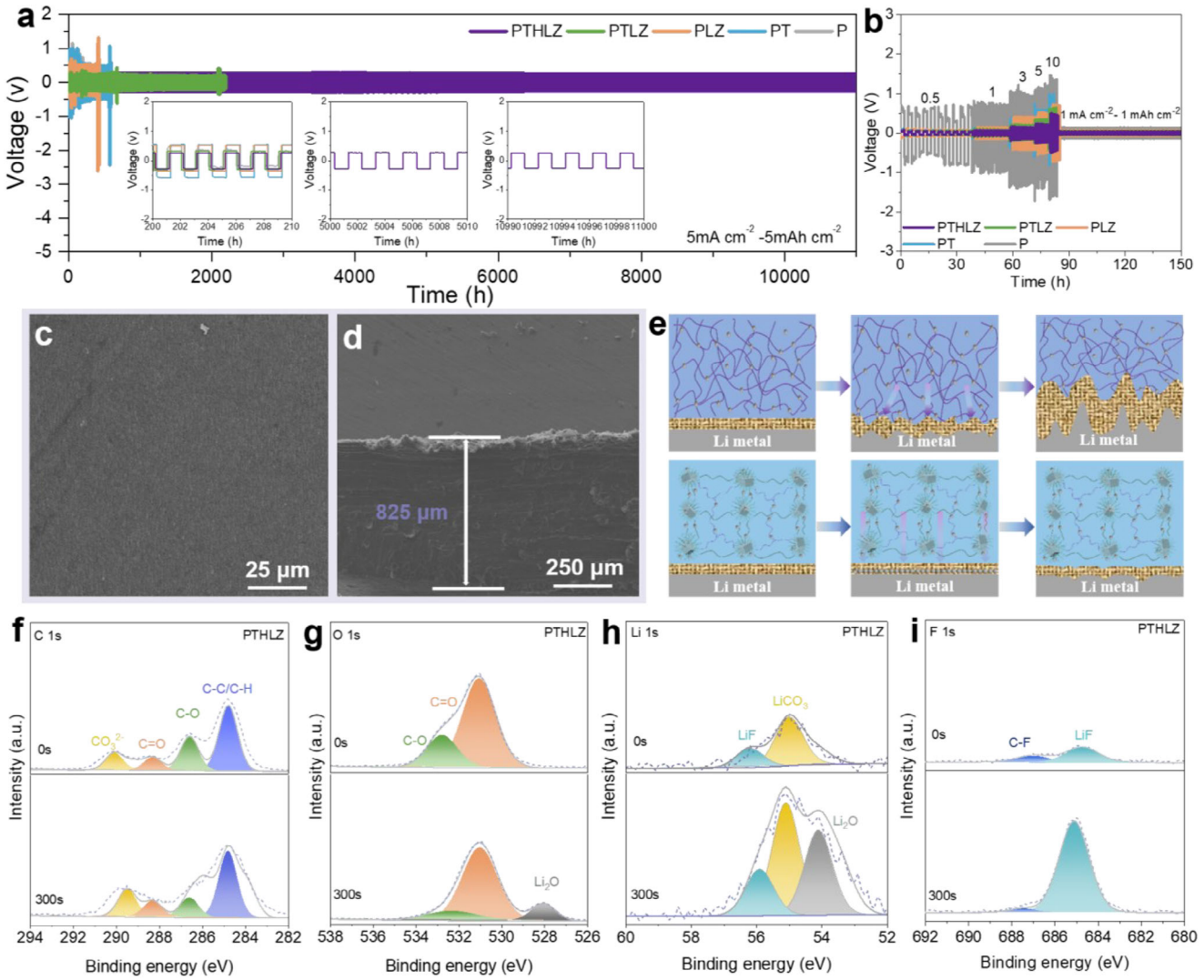

Figure 5. a) Long-term cycling performance of Li|Li symmetric cells in PTHLZ, PTLZ, PLZ, PT, and P at 5 mA cm^{-2} and 5 mAh cm^{-2} and magnification over different time periods. b) Rate performance of Li|Li symmetric cells with different quasi-solid electrolytes. SEM image of the surfaces c) and cross sections d) of the Li anode of the PTHLZ after 100 cycles of the Li||Li symmetric cells at 5 mA cm^{-2}. e) The Li^+ deposition pathways and states of linear polymer electrolytes and double crosslinked structured PTHLZ at the lithium metal anode interface. f–i) XPS depth profiles of C 1s, O 1s, Li 1s, and F 1s in lithium metal anode cycled in Li||Li cells with PTHLZ.

mer chains. In addition, the abundant channels and Lewis acid sites within LiZSM-5 can allow Li^+ migration while restricting PF_6^-, thereby improving the ion mobility number. Trimer-IEM-PEGDA forms another network structure that can conduct Li^+ rapidly due to its excellent polymer chain segments in the polymer phase conductivity. The network structure additionally restricts some PF_6^- movement, further increasing Li^+ migration speed. The inorganic and organic phases are tightly bound by covalent bonds, allowing both frameworks to form multiple continuous ion channels for rapid Li^+ transport. This structural integration plays a crucial role in the thermal stability, ionic conductivity, and electrochemical properties of PTHLZ.

To probe the interfacial stability during Li stripping/plating processes, Li|QSE|Li symmetric cells employing different electrolytes were systematically evaluated. Contact angle measurements reveal improved wettability of the liquid polymer precursor on separators, with uniform polymer infiltration into Li surfaces (Figure S33, Supporting Information). **Figure 5a** compares the cycling performance of Li|QSE|Li cells (PTHLZ, PTLZ, PLZ, PT, and P electrolytes) at 5 mA cm^{-2} with 1 h plating/stripping cycles. Cells using PTLZ, PLZ, PT, and P electrolytes exhibit progressively increasing polarization voltages (>500 mV), leading to premature short-circuiting within 500 h (PT, P) or 2200 h (PTLZ), attributed to uncontrolled Li dendrite propagation and dead Li accumulation. Notably, the PTHLZ-based cell maintains an ultralow polarization voltage (260 mV) with negligible fluctuation over record-breaking 11 000 h cycling, demonstrating exceptional interfacial stability. This performance stems from the mechanically reinforced dual-crosslinked network-combining LiZSM-5 surface grafting and Trimer-mediated crosslinking, which synergistically suppresses dendrite formation while enabling continuous 3D Li^+ transport channels. These channels not only

mitigate nanoparticle agglomeration but also ensure homogeneous Li deposition, significantly outperforming state-of-the-art solid electrolytes under high-current conditions (Table S2, Supporting Information). Polarization tests at increasing current densities (Figure S34, Supporting Information) confirm the stability of PTHLZ, maintaining consistent overpotentials through 4000 h at 10 mA cm^{-2}. In addition, EIS analysis (Figure S35, Supporting Information) reveals a minimal interfacial resistance increase (90 Ω) for PTHLZ after 100 cycles at 5 mA cm^{-2}, far surpassing counterparts: PHLZ (230 Ω), PLZ (397 Ω), PT (405 Ω), and P (894 Ω). To further evaluate the Li metal anode interfacial stability of the PTHLZ when the current is altered, the voltage profile of Li constant-current plating/stripping was tested when the current density increased from 0.5 to 10 mA cm^{-2} (Figure 5b). The polarization voltage becomes larger with increasing current density. Even at 10 mA cm^{-2}, the cell maintains stable cycling without short-circuiting, attributed to the rapid ion channels and high ionic conductivity of PTHLZ.[58] The polarization voltages of the cells with PTHLZ are 50, 95, 160, 260, and 510 mV at 0.5, 1, 3, 5, and 10 mA cm^{-2}, respectively, and still maintained stable cycling when the current density recovered from 10 to 1 mA cm^{-2}. In contrast, control cells (PTLZ, PLZ, PT, P) experience catastrophic failure at 10 mA cm^{-2} due to sluggish ion transport. To verify the inhibitory effect of PTHLZ on Li dendrites, the surface morphology of Li metal anodes of Li|PTHLZ|Li cells after 100 cycles was investigated by scanning electron microscopy (SEM) (Figure 5c,d). Post-cycling SEM characterization of PTHLZ-assembled Li anodes reveals smooth surfaces with negligible mossy Li formation, while cross-sectional analysis showed controlled thickness evolution (825 µm, Figure S36a,b, Supporting Information). Conversely, control electrolytes induced severe surface cracking and excessive dead Li layers (>825 µm, Figures S36c–h and S37c–j, Supporting Information), directly correlating with their rapid capacity decay. Figure 5e schematically contrasts Li^+ deposition pathways in linear polymer and dual-crosslinked (PTHLZ) systems. The 3D percolating ion channels in PTHLZ enable spatially uniform Li^+ flux, fostering stable SEI formation. This unique architecture endows PTHLZ with unparalleled electrochemical stability, paving the way for long-cycle-life and safe SSLMBs.

To further explore the formation and microstructural evolution of the SEI film, the spatial distribution of the chemical components in the SEI was characterized at different depths after 50 cycles using Ar^+ etching (Figure 5f–i). The high-resolution C 1s spectra reveal three characteristic peaks at 284.8, 286.6, 288.3, and 290.1 eV, corresponding to C—C/C—H, C—O, C═O, and CO_3^{2-} species, respectively, confirming the coexistence of organic and inorganic components in the SEI. A progressive decrease in C-related peak intensities with etching depth suggests a gradual reduction of organic constituents in inner SEI layers. Notably, the absence of Al 2p and Si 2p signals in XPS patterns (Figure S38, Supporting Information) confirms the electrochemical stability of LiZSM-5 without decomposition participation in SEI formation. In the O 1s and Li 1s spectra, the dominant peak at 55 eV corresponds to Li_2CO_3, indicating preferential formation of this inorganic component at the surface. As etching proceeds to deeper layers, emerging peaks at 528 eV, 54.1 eV (Li_2O) and 55 eV demonstrate forming Li_2O in the inner SEI and the continuous increase of $LiCO_3$ content, which contributes to higher coulombic efficiency in SSLMBs.[59] Remarkably, the F 1s and Li 1s spectra exhibit prominent LiF signals at 684.4 and 56.9 eV, respectively, with intensities showing positive correlation with etching depth. The proportion of inorganic components (Li_2CO_3, LiF, and Li_2O) in the inner layers of the SEI formed with PTHLZ substantially increases, which indicates that inorganic components dominate the inner SEI in PTHLZ, contributing to enhanced cell stability and cycling performance.[60–62]

To evaluate the electrochemical performance of different electrolytes, full cells incorporating high-mass-loading LFP and NCM811 cathodes were comprehensively investigated. As demonstrated in **Figure 6**a, the LFP|PTHLZ|Li cell delivers a remarkable initial discharge capacity of 144.9 mAh g^{-1} at 1C, maintaining 63.6% capacity retention after 1200 cycles with superior cycling stability. This performance significantly surpasses that of cells employing PTLZ, PLZ, PT, and P electrolytes, which suffer from inferior initial capacities and unstable coulombic efficiency due to suboptimal ionic conductivity and nonuniform SEI formation. Notably, the irregular SEI morphology induces sluggish Li^+ transport kinetics, progressively increasing polarization, thereby accelerating capacity degradation. The exceptional electrochemical stability of PTHLZ-based cells is further evidenced by the minimal voltage hysteresis between charge/discharge plateaus from the 1st to 1200 cycle (Figure 6b). In sharp contrast, cells with other electrolytes exhibit exponentially growing polarization with cycling (Figure S39, Supporting Information), implying very small and stable polarization, excellent ionic conductivity of the PTHLZ, as well as low interfacial impedance. To evaluate the cycling stability under high current conditions, a long-term cycling test is performed at 5 C (Figure S40, Supporting Information). The PTHLZ electrolyte exhibits stable cycling over 400 cycles with a capacity retention of 50%. In addition, rate capability evaluation (Figure 6c,d) reveals that PTHLZ-based cells achieve 164.4 mAh g^{-1} at 0.1 C, retaining 60.6 mAh g^{-1} at 5 C when returning to 0.2 C (156.4 mAh g^{-1}). Comparatively, other electrolyte systems show rapid performance deterioration above 0.5 C and complete failure at 5 C (Figure S41, Supporting Information). The experimental results show that PTHLZ cells with in situ polymerization interface and dual crosslinked strategy have stable high-current charging and discharging performance and high reversibility. As a result, PTHLZ shows marked improvements over existing in situ polymerized solid electrolytes, with enhanced temperature adaptability, capacity retention, cycle longevity, rate, and area loading capabilities relative to reported composite solid electrolytes (Figure 6e).

To further evaluate the applicability of the PTHLZ electrolyte in high-energy-density batteries, NCM811|Li cells with high mass loading (17.5 mg cm^{-2}) were investigated. As shown in Figure 6f, the NCM811|PTHLZ|Li cell maintains a discharge capacity of 120 mAh g^{-1} with 72.3% capacity retention after 800 cycles at 0.5 C, accompanied by highly reversible charge/discharge profiles (Figure 6g). However, the NCM811|PT|Li cell (best-performing control) exhibits rapid capacity fade from 168.3 to 97.7 mAh g^{-1} (58.1% retention) within merely 300 cycles (Figure S42, Supporting Information). This marked superiority originates from the Trimer-based molecular design enabling superior ion transport and the dual-crosslinked architecture formed by HEYTS-LiZSM-5 and Trimer, which synergistically enhances high-voltage tolerance. Notably, the in situ polymer-

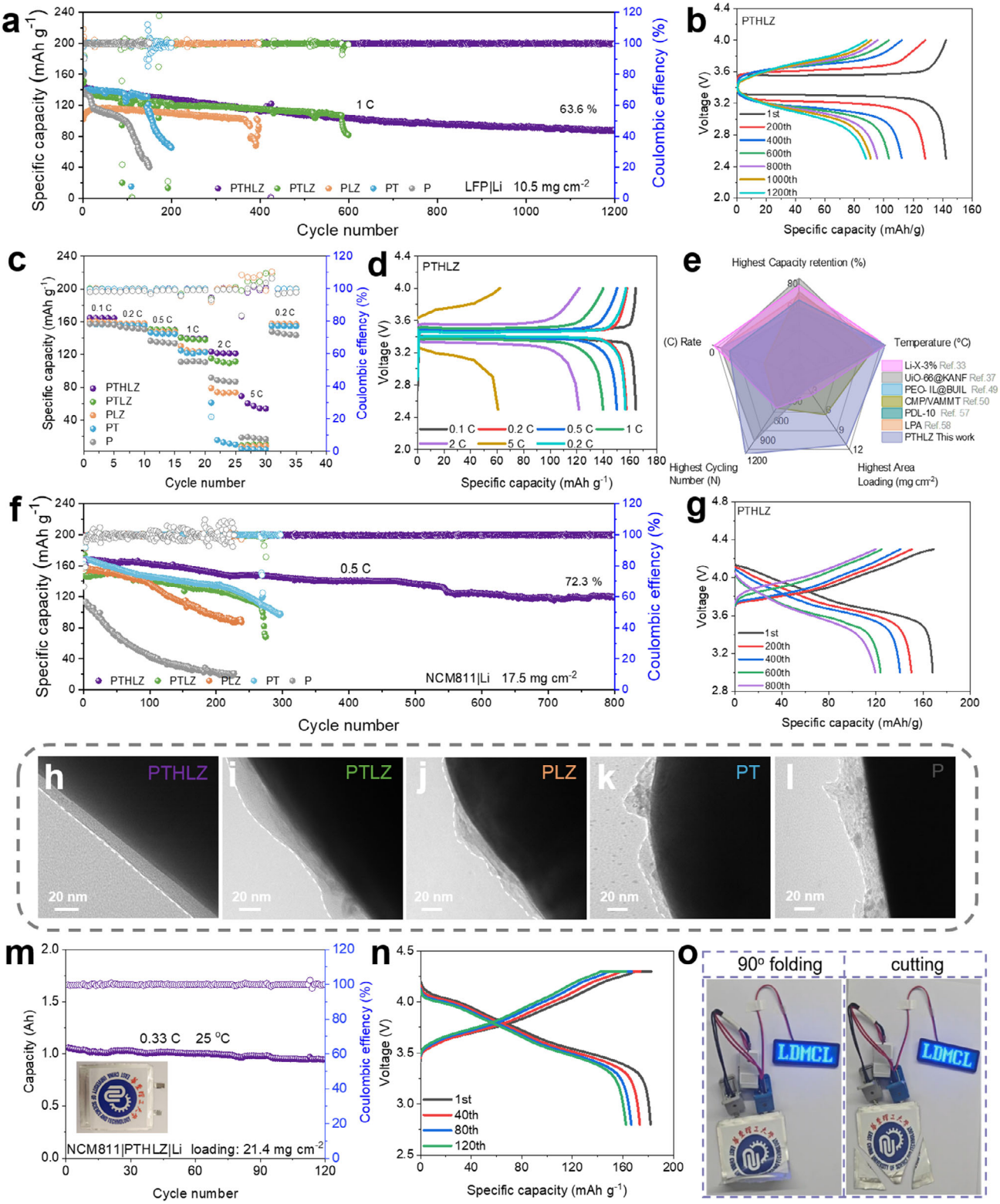

Figure 6. Application of PTHLZ electrolyte in lithium metal battery. a) Cycling performance of LFP|QSE|Li at 1 C. b) The corresponding charge/discharge profiles at different cycles of PTHLZ-based LFP|Li cell. c) Rate performance of LFP|PTHLZ|Li cells at different rates. d) Charge/discharge curves of LFP|PTHLZ|Li cell in the first turn at each rate. e) Radar plots that compare the electrochemical performance of various reported works. f) Cycling performance of NCM811|QSE|Li cell at 0.5 C. g) Charge/discharge curves of NCM811|PTHLZ|Li cell. h–l) High-resolution TEM images of NCM811 particles after full cell cycling with different solid electrolytes. m) Cycling performance of NCM811|PTHLZ|Li soft pack battery at 0.33 C. n) Voltage capacity curves of NCM811|PTHLZ|Li soft pack battery with different numbers of turns. o) The abuse experiment of NCM811|PTHLZ|Li soft pack battery.

ized PTHLZ establishes exceptional antioxidant stability and intimate cathode-electrolyte interfacial compatibility. TEM analysis (Figure 6h) reveals an ultrathin and homogeneous CEI layer on cycled NCM811 particles in PTHLZ-based cells, effectively suppressing electrolyte decomposition and indicating excellent interfacial compatibility of PTHLZ. This performance surpasses that reported in the current literature (Table S4, Supporting Information). In contrast, cells with PTLZ, PLZ, PT, and P electrolytes form a nonuniform and thicker CEI layer (Figure 6i–l), which leads to higher interfacial resistance at the cathode/electrolyte interface and slower ion transport. The essential reason for the poor cycling performance of their corresponding batteries can also be demonstrated laterally. To further explore the practical feasibility of PTHLZ, an Ah-level soft pack battery was prepared, and the electrochemical performance was evaluated. As shown in Figure 6m,n, the NCM811 anode with higher loading (21.4 mg cm^{-2}) delivers a high capacity of 1 Ah at room temperature and still achieves very stable cycling performance with 89.2% capacity retention after 120 cycles. And impressively, the soft pack battery is also able to withstand rigorous cutting and severe folding tests, as shown in Figure 6o and Video S1 (Supporting Information), illustrating the remarkable safety and stability of the PTHLZ electrolyte in SSLMBs. In conclusion, these findings demonstrate favorable practical application potentials of PTHLZ as a solid electrolyte for high-performance and durable SSLMBs.

3. Conclusion

In summary, we present a kind of dual-crosslinked solid electrolyte (PTHLZ) engineered through in situ polymerization of vinyl-functionalized LiZSM-5 nanoparticles and hemiacetal amine-based Trimer, constructing a 3D network with multiple continuous Li^+ transport channels. This molecularly tailored architecture delivers excellent ionic conductivity (3.7 mS cm^{-1}) and Li^+ transference number ($t_{Li}{}^+ = 0.89$), enabled by synergistic effects of strongly dissociated flexible chains and Lewis acid-base interactions at LiZSM-5 interfaces. Multiple fast transport channels enable Li|Li symmetric cells to operate under dendrite-free operation for more than 11 000 h by accelerating Li^+ desorption kinetics. Practical implementations demonstrate favorable cyclability: high-loading LFP|PTHLZ|Li cells retain 63.6% capacity after 1200 cycles at 1 C, while NCM811|PTHLZ|Li cells maintain 72.3% retention over 800 cycles at 0.5 C. Remarkably, Ah-level pouch cells achieve 89.2% capacity retention post 120 cycles with inherent safety against mechanical abuse. Our proposed CQSEs based on in situ dual crosslinked centers provide a promising and scalable platform for designing high-performance SSLMBs.

Supporting Information

Supporting Information is available from the Wiley Online Library or from the author.

Acknowledgements

H.L. and D.L. contributed equally to this work. This work was funded by the Shanghai Pilot Program for Basic Research (22TQ1400100-13). The Leading Talents in Shanghai in 2018. The 111 project (B14018).

Conflict of Interest

The authors declare no conflict of interest.

Data Availability Statement

Research data are not shared.

Keywords

composite quasi-solid electrolyte, high-loading electrode, in situ polymerization, ultra-long cycle, zeolite

Received: March 10, 2025
Revised: June 10, 2025
Published online:

[1] J. Tao, D. Wang, Y. Yang, J. Li, Z. Huang, S. Mathur, Z. Hong, Y. Lin, *Adv. Sci.* **2022**, *9*, 210378.
[2] U. Pal, D. Rakov, B. Lu, B. Sayahpour, F. Chen, B. Roy, D. R. MacFarlane, M. Armand, P. C. Howlett, Y. S. Meng, M. Forsyth, *Energy Environ. Sci.* **2022**, *15*, 1907.
[3] D. Chen, M. Zhu, P. Kang, T. Zhu, H. Yuan, J. Lan, X. Yang, G. Sui, *Adv. Sci.* **2021**, *9*, 210366.
[4] Y. Guo, H. Li, T. Zhai, *Adv. Mater.* **2017**, *29*, 1700007.
[5] M. B. Dixit, W. Zaman, N. Hortance, S. Vujic, B. Harkey, F. Shen, W.-Y. Tsai, V. De Andrade, X. C. Chen, N. Balke, K. B. Hatzell, *Joule* **2020**, *4*, 207.
[6] Y. Wang, X. Guo, Z. Lin, Y. Yang, L. Wu, H. Liu, H. Yu, *Chem. Res. Chinese U.* **2020**, *36*, 439.
[7] Z. Lin, X. Guo, Z. Wang, B. Wang, S. He, L. A. O Dell, J. Huang, H. Li, H. Yu, L. Chen, *Nano Energy* **2020**, *73*, 104786.
[8] R. Li, H. Hua, X. Yang, J. Tian, Q. Chen, R. Huang, X. Li, P. Zhang, J. Zhao, *Energy Environ. Sci.* **2024**, *17*, 5601.
[9] Z. Jia, M. Jia, Q. Sun, N. Wang, Z. Bi, X. Guo, *Energy Storage Mater.* **2024**, *68*, 103325.
[10] R. Murugan, V. Thangadurai, W. Weppner, *Angew. Chem. Inter. Ed.* **2007**, *46*, 7778.
[11] S. Luo, Z. Wang, X. Li, X. Liu, H. Wang, W. Ma, L. Zhang, L. Zhu, X. Zhang, *Nat. Commun.* **2021**, *12*, 6968.
[12] N. Meng, Y. Ye, Z. Yang, H. Li, F. Lian, *Adv. Funct. Mater.* **2023**, *33*, 2305072.
[13] J. Chen, X. Deng, Y. Gao, Y. Zhao, X. Kong, Q. Rong, J. Xiong, D. Yu, S. Ding, *Angew. Chem. Inter. Ed.* **2023**, *62*, 202307255.
[14] J. Gou, Z. Zhang, S. Wang, J. Huang, K. Cui, H. Wang, *Adv. Mater.* **2023**, *36*, 2309677.
[15] M. Liu, S. Zhang, E. R. H. van Eck, C. Wang, S. Ganapathy, M. Wagemaker, *Nat. Nanotechnol.* **2022**, *17*, 959.
[16] T. Zhang, J. Li, X. Li, R. Wang, C. Wang, Z. Zhang, L. Yin, *Adv. Mater.* **2022**, *34*, 2205575.
[17] J. C. Bachman, S. Muy, A. Grimaud, H.-H. Chang, N. Pour, S. F. Lux, O. Paschos, F. Maglia, S. Lupart, P. Lamp, L. Giordano, Y. Shao-Horn, *Chem. Rev.* **2015**, *116*, 140.
[18] J. Zheng, Y.-Y. Hu, *ACS Appl. Mater. Interfaces* **2018**, *10*, 4113.
[19] S. Ramesh, S. Lu, *J. Power Sources* **2008**, *185*, 1439.
[20] Y. Shi, Z. Fan, B. Ding, Z. Li, Q. Lin, S. Chen, H. Dou, X. Zhang, *J. Electroanal. Chem.* **2021**, *881*, 114916.
[21] Z. Xu, T. Yang, X. Chu, H. Su, Z. Wang, N. Chen, B. Gu, H. Zhang, W. Deng, H. Zhang, W. Yang, *ACS Appl. Mater. Interfaces* **2020**, *12*, 10341.
[22] Y. L. Ni'mah, Z. H. Muhaiminah, S. Suprapto, *Polymers* **2021**, *13*, 4240.

[23] C. Yuan, J. Li, P. Han, Y. Lai, Z. Zhang, J. Liu, *J. Power Sources* **2013**, *240*, 653.
[24] U. Kokçam-Demir, A. Goldman, L. Esrafili, M. Gharib, A. Morsali, O. Weingart, C. Janiak, *Chem. Soc. Rev.* **2020**, *49*, 2751.
[25] H. He, N. Deng, X. Wang, L. Gao, C. Tang, E. Wu, J. Ren, X. Yang, N. Feng, D. Gao, X. Zhuang, *Adv. Funct. Mater.* **2025**, *35*, 2421670.
[26] J. Zhang, Y. Wang, Q. Xia, X. Li, B. Liu, T. Hu, M. Tebyetekerwa, S. Hu, R. Knibbe, S. Chou, *Angew. Chem., Int. Ed.* **2024**, *136*, 202318822.
[27] Y. Yang, Z. Sun, Y. Wu, Z. Liang, F. Li, M. Zhu, J. Liu, *Small* **2024**, *20*, 2401457.
[28] J. Barbosa, D. Correia, P. Nunes, M. Fernandes, A. Fidalgo-Marijuan, R. Gonçalves, S. Ferdov, V. Bermudez, S. Lanceros-Mendez, C. Costa, *J. Power Sources* **2023**, *572*, 233095.
[29] G. Zhang, Y. Hong, Y. Nishiyama, S. Bai, S. Kitagawa, S. Horike, *J. Am. Chem. Soc.* **2018**, *141*, 1227.
[30] X. X. Wang, X. W. Chi, M. L. Li, D. H. Guan, C. L. Miao, J. J. Xu, *Adv. Funct. Mater.* **2022**, *32*, 2113235.
[31] X. Chi, M. Li, J. Di, P. Bai, L. Song, X. Wang, F. Li, S. Liang, J. Xu, J. Yu, *Nature* **2021**, *592*, 551.
[32] L. Zheng, P. Bai, W. Yan, F. Li, X. Wang, J. Xu, *Matter* **2023**, *6*, 142.
[33] Z. Ding, Q. Tang, Q. Zhang, P. Yao, X. Liu, J. Wu, *Nano Res.* **2023**, *16*, 9443.
[34] M. Shen, Z. Wang, D. Cheng, H. Cheng, H. Xu, Y. Huang, *eTransportation* **2023**, *18*, 100264.
[35] H. Wang, F. Liu, R. Yu, J. Wu, *Int. Mater.* **2022**, *1*, 196.
[36] Y. Wang, L. Wu, Z. Lin, M. Tang, P. Ding, X. Guo, Z. Zhang, S. Liu, B. Wang, X. Yin, Z. Chen, K. Amine, H. Yu, *Nano Energy* **2022**, *96*, 107105.
[37] Y. Liu, S. Wang, W. Chen, W. Kong, S. Wang, H. Liu, L. Ding, L. X. Ding, H. Wang, *Adv. Mater.* **2024**, *36*, 2401837.
[38] S. Ramesh, L. C. Wen, *Ionics* **2009**, *16*, 255.
[39] J. Zagorski, J. M. Lopez del Amo, M. J. Cordill, F. Aguesse, L. Buannic, A. Llordes, *ACS Appl. Energy Mater.* **2019**, *2*, 1734.
[40] J. Bae, Y. Li, J. Zhang, X. Zhou, F. Zhao, Y. Shi, J. B. Goodenough, G. Yu, *Angew. Chem., Int. Ed.* **2018**, *57*, 2096.
[41] N. W. Utomo, Y. Deng, Q. Zhao, X. Liu, L. A. Archer, *Adv. Mater.* **2022**, *34*, 2110333.
[42] C. Z. Zhao, Q. Zhao, X. Liu, J. Zheng, S. Stalin, Q. Zhang, L. A. Archer, *Adv. Mater.* **2020**, *32*, 1905629.
[43] G. Liu, Z. Cao, P. Wang, Z. Ma, Y. Zou, Q. Sun, H. Cheng, L. Cavallo, S. Li, Q. Li, J. Ming, *Adv. Sci.* **2022**, *9*, 2201893.
[44] Z. Sun, K. Xi, J. Chen, A. Abdelkader, M.-Y. Li, Y. Qin, Y. Lin, Q. Jiang, Y. Q. Su, R. Vasant Kumar, S. Ding, *Nat. Commun.* **2022**, *13*, 3209.
[45] X. Chi, M. Li, X. Chen, J. Xu, X. Yin, S. Li, Z. Jin, Z. Luo, X. Wang, D. Kong, M. Han, J.-J. Xu, Z. Liu, D. Mei, J. Wang, G. Henkelman, J. Yu, *J. Am. Chem. Soc.* **2023**, *145*, 24116.
[46] Z. Jin, L. Wang, E. Zuidema, K. Mondal, M. Zhang, J. Zhang, C. Wang, X. Meng, H. Yang, C. Mesters, F. Xiao, *Science* **2020**, *367*, 193.
[47] J. Zhou, S. Wu, F. Chu, Z. Jiang, F. Wu, *Adv. Funct. Mater.* **2025**, *35*, 2423742.
[48] S. Ye, Y. Zhang, Y. Huang, Y. Li, Z. Li, C. Ou, M. Lin, F. Tian, D. Lei, C. Wang, *Angew. Chem., Int. Ed.* **2025**, 202506662, https://doi.org/10.1002/anie.202506662.
[49] Y. Song, H. Qu, Z. Lao, X. Xiao, G. Lu, Y. Song, L. Nie, J. Wang, J. Yang, Y. Zhu, G. Zhou, *Adv. Mater.* **2025**, *37*, 2419271.
[50] X. Li, Y. Wang, K. Xi, W. Yu, J. Feng, G. Gao, H. Wu, Q. Jiang, A. Abdelkader, W. Hua, G. Zhong, S. Ding, *Nano-Micro Lett.* **2022**, *14*, 210.
[51] L. Zhang, P. Zhang, C. Chang, W. Guo, Z. H. Guo, X. Pu, *ACS Appl. Mater. Interfaces* **2021**, *13*, 46794.
[52] Y. Ren, S. Chen, M. Odziomek, J. Guo, P. Xu, H. Xie, Z. Tian, *Angew. Chem., Int. Ed.* **2025**, *64*, 202422169.
[53] J. Guo, F. Feng, S. Zhao, R. Wang, M. Yang, Z. Shi, Y. Ren, Z. Ma, S. Chen, T. Liu, *Small* **2023**, *19*, 2206740.
[54] N. S. Grundish, C. D. Amos, A. Agrawal, H. Khani, J. B. Goodenough, *Adv. Funct. Mater.* **2019**, *29*, 1903550.
[55] L. Chen, W. Li, L. Z. Fan, C. W. Nan, Q. Zhang, *Adv. Funct. Mater.* **2019**, *29*, 1901047.
[56] Q. Lu, C. Wang, D. Bao, H. Duan, F. Zhao, K. Doyle-Davis, Q. Zhang, R. Wang, S. Zhao, J. Wang, H. Huang, X. Sun, *Energy Environ. Mater.* **2023**, *6*, 12447.
[57] Y. Zhao, L. Li, D. Zhou, Y. Ma, Y. Zhang, H. Yang, S. Fan, H. Tong, S. Li, W. Qu, *Angew. Chem., Int. Ed.* **2024**, *63*, 202404728.
[58] Y. Li, S. Ma, Y. Zhao, S. Chen, T. Xiao, H. Yin, H. Song, X. Pan, L. Cong, H. Xie, *Energy Environ. Mater.* **2024**, *7*, 12648.
[59] C. Shen, W. Feng, Y. Yu, H. Wang, Y. Cheng, C. Dong, J. Gu, A. Zheng, X. Liao, X. Xu, L. Mai, *Adv. Energy Mater.* **2024**, *14*, 2304511.
[60] S. J. Yang, N. Yao, F. N. Jiang, J. Xie, S. Y. Sun, X. Chen, H. Yuan, X. B. Cheng, J. Q. Huang, Q. Zhang, *Angew. Chem., Int. Ed.* **2022**, *61*, 202214545.
[61] Y. Liu, X. Tao, Y. Wang, C. Jiang, C. Ma, O. Sheng, G. Lu, X. W. D. Lou, *Science* **2022**, *375*, 739
[62] J. Yang, M. Li, Z. Sun, X. Lian, Y. Wang, Y. Niu, C. Jiang, Y. Luo, Y. Liu, Z. Tian, Y. Long, K. Zhang, P. Yu, J. Zhang, Z. Wang, G. Wu, M. Gu, W. Chen, *Energy Environ. Sci.* **2023**, *16*, 3837.